Nanoscale

PAPER

View Article Online
View Journal | View Issue

Cite this: *Nanoscale*, 2017, **9**, 18788

Photo-degradation of high efficiency fullerene-free polymer solar cells†

Mushfika Baishakhi Upama, * Matthew Wright, Md Arafat Mahmud, Naveen Kumar Elumalai, * Arman Mahboubi Soufiani, Dian Wang, Cheng Xu and Ashraf Uddin

Received 18th August 2017,
Accepted 8th November 2017

DOI: 10.1039/c7nr06151j

rsc.li/nanoscale

Polymer solar cells are a promising technology for the commercialization of low cost, large scale organic solar cells. With the evolution of high efficiency (>13%) non-fullerene polymer solar cells, the stability of the cells has become a crucial parameter to be considered. Among the several degradation mechanisms of polymer solar cells, burn-in photo-degradation is relatively less studied. Herein, we present the first systematic study of photo-degradation of novel PBDB-T:ITIC fullerene-free polymer solar cells. The thermally treated and as-prepared PBDB-T:ITIC solar cells were exposed to continuous 1 sun illumination for 5 hours. The aged devices exhibited rapid losses in the short-circuit current density and fill factor. The severe short-circuit current and fill factor burn in losses were attributed to trap mediated charge recombination, as evidenced by an increase in Urbach energy for aged devices.

1 Introduction

Solution processed polymer solar cells (PSCs) are an attractive renewable energy technology, as they are lightweight,[1] transparent,[2,3] flexible,[4] less expensive and easy-to-fabricate and can be installed with roll-to-roll processing compatibility.[5–7] Recently, single junction bulk heterojunction PSCs have achieved power conversion efficiency (PCE) exceeding 13%.[8] This impressive PCE was achieved by replacing the traditional fullerene acceptors, such as PCBM and ICBA,[9–11] with non-fullerene, small molecule acceptors.[8] Fullerene acceptors have some inherent drawbacks, such as limited light absorption,[12] high synthetic cost,[13] and limited tunability of the electronic energy levels.[14] These factors strongly limit the photovoltaic performance of polymer : fullerene solar cells. In contrast, non-fullerene acceptors have strong absorption in the visible solar spectrum, easily tunable energy levels and low-cost processing.[15,16] As a result, non-fullerene acceptors are becoming widely popular in high performance PSC design and engineering. In particular, efficient large π-conjugation acceptor–donor–acceptor (A–D–A) acceptors, such as 3,9-bis(2-methylene-(3-(1,1-dicyanomethylene)-indanone))-5,5,11,11-tetrakis(4-hexylphenyl)-dithieno[2,3-*d*:2′,3′-*d*′]-*s*-indaceno[1,2*b*:5,6-*b*′]dithiophene (ITIC), possess broad and strong absorption, good electron transport capability, low lowest unoccupied molecular orbital (LUMO) and highest occupied molecular orbital (HOMO) energy levels, and good miscibility with polymer donors.[17] Zhao *et al.*[18] have recently designed a new high performance polymer : non-fullerene bulk heterojunction (BHJ) solar cell with a conjugated polymer (PBDB-T: poly[(2,6-(4,8-bis(5-(2-ethylhexyl)thiophen-2-yl)-benzo[1,2-*b*:4,5-*b*′]dithiophene))-*alt*-(5,5-(1′,3′-di-2-thienyl-5′,7′-bis(2-ethylhexyl)benzo[1′,2′-*c*:4′,5′-*c*′]dithiophene-4,8-dione))]) and ITIC, having complementary absorption spectra, that yielded >11% PCE.

In addition to a high PCE, the successful commercialization of polymer solar cells also depends on the stability of the device and processing techniques.[19] Several degradation factors affect the stability of PSCs, including the chemical[20] and photo-instability[19] of the light absorbing medium, oxidation,[19,21] thermally induced phase changes[22] and even, degradation of interfacial layers.[23,24] To date, PBDB-T:ITIC devices have displayed excellent thermal stability compared to PBDB-T:$PC_{71}BM$ devices due to the inherent stability of the ITIC non-fullerene acceptor.[18] Apart from thermal stability, non-fullerene acceptors have also showcased good stability in ambient air[25] and long-term stability under dark storage conditions.[26] However, unlike fullerene based PSCs,[23,27] the photo-stability of non-fullerene PSC is still not well-investigated. To enhance the operational lifetime of non-fullerene PSCs, the photo-stability of the polymer : non-fullerene BHJ system needs to be well analyzed and understood. The photo-degradation constitutes the rapid reduction in the overall

School of Photovoltaic and Renewable Energy Engineering, University of New South Wales, 2052 Sydney, Australia. E-mail: m.upama@student.unsw.edu.au, n.elumalai@unsw.edu.au

†Electronic supplementary information (ESI) available. See DOI: 10.1039/c7nr06151j

photovoltaic performance of the organic devices, such as PSCs, under continuous illumination, termed 'burn-in' degradation.[24,28] The burn-in test is typically conducted by the manufacturers of electronic devices with fast initial failure,[24,29] in order to confirm the reliability of the product to the customer. The initial degradation or burn-in in PSCs is also required to be tested for successful application of this new and promising technology in the form of organic photovoltaic modules. Understanding the burn-in losses will be a crucial step toward addressing the issue of stability, reliability and commercialization of organic photovoltaics. Despite its importance, the short-term photo-stability is not frequently included in the device stability studies. It is important to address the burn-in degradation in order to mitigate the loss of a particular BHJ solar cell system; otherwise the device efficiency can be greatly reduced[24] in the initial stages of operation even though its initial efficiency is high. Voroshazi *et al.*[30] reported that the burn-in process in PSCs is material dependent, hence the burn-in study needs to be conducted for individual systems to find the origin of the process. Hence, an intensive burn-in degradation study is required for non-fullerene solar cell systems. The current study aims to understand the origin of burn-in degradation in non-fullerene solar cell systems using photothermal deflection spectroscopy (PDS). PDS is a sensitive technique which allows for the study of the sub-bandgap absorption in a semiconductor. Doing so provides insights into the structural disorder in the film, as well as the formation of trap states. This tool has been previously used to investigate the origin of burn-in phenomena in polymer : fullerene solar cells.[27,31]

We present a systematic study of the mechanisms causing burn-in degradation in PBDB-T:ITIC, a non-fullerene based PSC. We fabricated high efficiency (PCE > 11%) PBDB-T:ITIC solar cells by spin-coating and investigated the initial photo-degradation of the device structure. Both thermally annealed and non-annealed devices were fabricated in order to investigate the effect of thermal annealing on the burn-in effect. In both types of devices, a high burn-in loss was observed in all photovoltaic parameters at room temperature, which was found to be associated with an increase in sub-bandgap absorption and Urbach energy of the active layer BHJ blend, measured using PDS, although the annealed devices exhibited a slightly lower burn-in loss. We employed PDS to measure the sub-bandgap absorption and examine the possible trap formation in the active layer due to photochemical reactions. In addition, electrochemical impedance spectroscopy (EIS) and steady-state photoluminescence (PL) were conducted to provide a more complete picture of the burn-in phenomenon.

2 Experimental details

2.1 Device fabrication

The chemical structures of the polymer donor, PBDB-T, and non-fullerene acceptor, ITIC, are depicted in Fig. 1a and b. Fig. 1c illustrates the inverted device architecture, in which solution-processed ZnO and thermally evaporated MoO_3 are employed as n- and p-type interfacial layers, respectively. Indium tin oxide (ITO) and silver (Ag) are the cathode and anode, respectively. ITO-coated glass substrates (12 mm × 12 mm) were used for all devices. Quartz substrates were used to prepare PDS samples. The substrates were first cleaned by ultrasonication in soapy deionized (DI) water, DI water, acetone, and isopropanol. ZnO sol–gel solution (0.48 M) was prepared by following the procedures from our previous reports.[3,32,33] It was then spin-cast on top of the pre-cleaned ITO glass substrates at 4000 rpm for 60 s. These samples were then annealed at 170 °C for 30 min. PBDB-T and ITIC (purchased from Solarmer Materials Inc.) were mixed (1 : 1 weight ratio) in a 20 mg mL^{-1} chlorobenzene : DIO (99.5 : 0.5) solution in a N_2-filled glovebox and stirred overnight at 50 °C. The solution was spin-coated on top of ZnO at 2500 rpm for 1 min to obtain an approx. 100 nm thick active layer. PDS samples were prepared by spin-coating the same solution directly on the quartz substrates. The coated ITO/glass substrates were loaded into a vacuum chamber at a pressure of 10^{-4} Pa, where a 10 nm film of MoO_3 and 100 nm film of silver were deposited through a shadow mask by thermal evaporation. The device area used was 0.12 cm^2. Then, half of the devices and films were annealed at 80 °C. At least ten devices were fabricated under annealed and non-annealed conditions.

2.2 Device characterization

The current density–voltage (*J–V*) measurements were performed using a solar cell *I–V* testing system from PV Measurements, Inc. (using a Keithley 2400 source meter) under an illumination power of 100 mW cm^{-2} by using an AM 1.5G solar simulator. To track the hourly burn-in photo-degradation, the devices and films were illuminated by using the same simulated sunlight source at 1 sun intensity in encapsulation and under open-circuit conditions. The test was conducted in the first 5 hours of the device operation, during which time the photo-induced degradation is most severe. The PSCs were encapsulated during the measurement to avoid exposure to external factors such as moisture and oxygen. The device temperatures were measured by using a GM1350 50 : 1 LCD Infrared Thermometer Digital Gun. In order to minimize thermally induced degradation effects, the temperature was maintained at near room temperature (35–40 °C) by forced air cooling during the aging process. For optical characterization, a UV–VIS-NIR spectrometer (PerkinElmer – Lambda 950) was used. For PDS measurements, the excitation light source or the pump beam was the output from a 250 W QTH lamp spectrally filtered by using a CornerstoneTM 130 monochromator. The output of the monochromator was further filtered with order sorting filters. A probe laser beam of 635 nm was used in conjunction with a four quadrant position detector to detect the beam deflection caused by the heat gradient. The sample was immersed in a Fluorinert FC72TM in a quartz cuvette. An ANFATECTM lock-in amplifier connected to a computer was used to record the deflection data at each wavelength. The

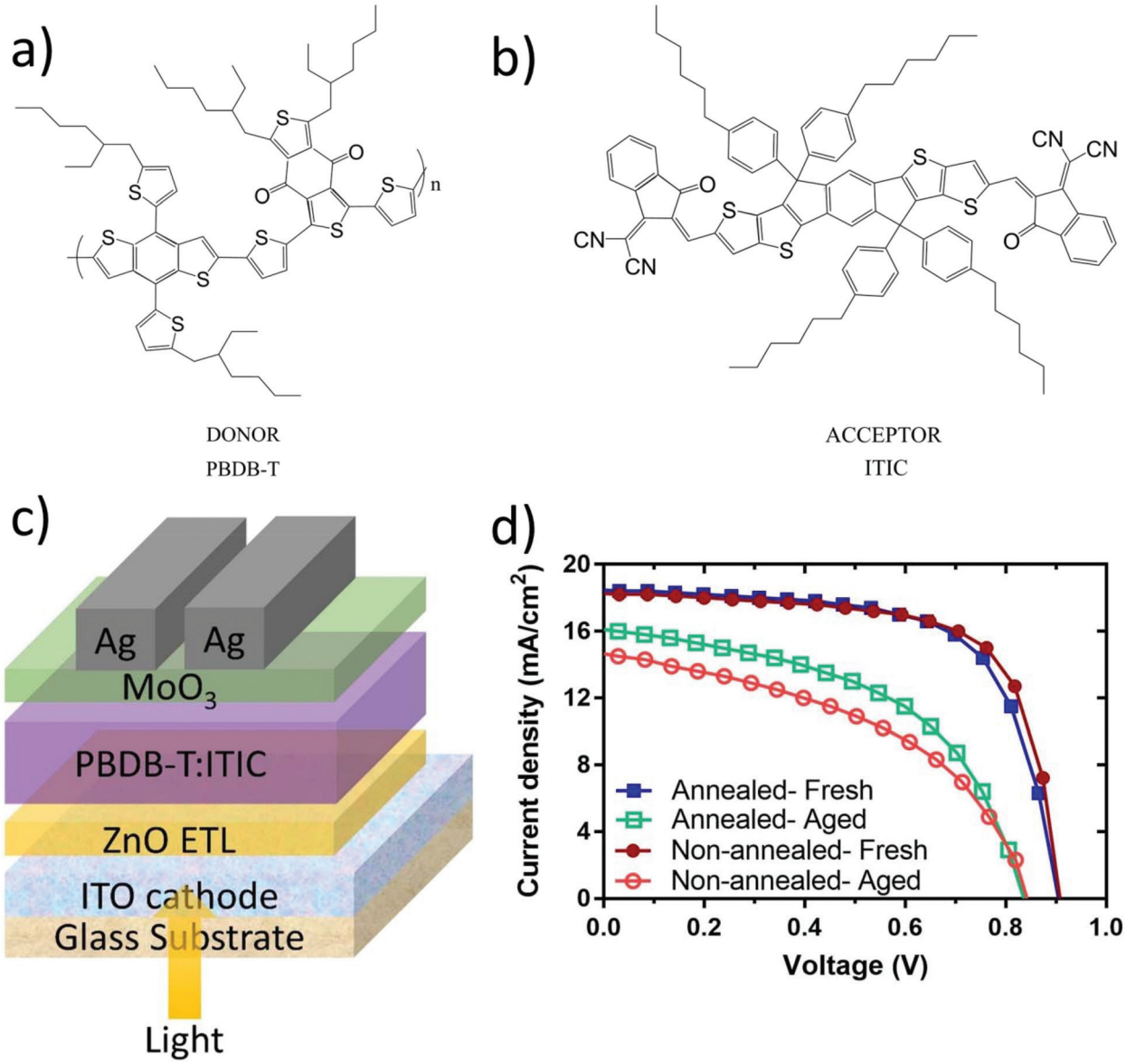

Fig. 1 (a, b) Chemical structures of active layer materials (donor polymer: PBDB-T and non-fullerene acceptor: ITIC, respectively); (c) schematic diagram of the inverted device structure; (d) current density–voltage characteristics of the fabricated non-annealed and annealed solar cells at room temperature under AM1.5G illumination at 100 mW cm^{-2}, before and after photo-degradation (labeled as 'fresh' and 'aged', respectively).

impedance and Mott–Schottky measurements were performed with an Autolab PGSTAT-30 equipped with a frequency analyser module in the frequency range of 10^6–100 Hz. The AC oscillating amplitude was as low as 20 mV (rms) to maintain the linearity of the response. PL spectra were measured using a 1/4 meter monochromator (CornerstoneTM 260) equipped with a silicon charge-coupled device (CCD) camera. The continuous wave laser (409 nm, 60 mW) was used in conjunction with optical density filters (to tune the excitation intensity) as the excitation source and the luminescence was detected by using the CCD. The laser lines were filtered out from the detected signal by using a 442 nm low pass filter. All the spectra were collected using a 2 second integration time.

3 Results and discussion

All devices investigated in this work were fabricated by spin-coating the active layer in a nitrogen-filled glovebox under optimized processing conditions. In order to explore the effect of thermal annealing on the burn-in effect, half of the fabricated devices were annealed at 80 °C. The annealing temperature was limited to 80 °C since the photovoltaic performance of the devices decreased sharply when the annealing temperature exceeded 100 °C. The photovoltaic performances of the fabricated PBDB-T:ITIC annealed at different temperatures are listed in Table S1.† Henceforth, the term 'annealed devices' indicates the devices annealed at 80 °C. The as-fabricated PSCs, labeled as 'fresh', were evaluated immediately after fabri-

Table 1 Photovoltaic performance parameters of the non-annealed and annealed OSCs under both fresh and aged conditions under AM1.5G 100 mW cm^{-2} illumination. Averages are based on at least ten cells

Device description	J_{sc} (mA cm^{-2})	V_{oc} (V)	FF (%)	PCE (%)	R_s (Ω cm^2)	R_{sh} (Ω cm^2)
Non-annealed (fresh)	18.3 ± 0.12	0.912 ± 0.00	68.8 ± 0.11	11.5 ± 0.06	4.7 ± 0.07	939 ± 104
Non-annealed (aged)	14.5 ± 0.22	0.836 ± 0.01	45.4 ± 1.41	5.5 ± 0.29	10 ± 0.47	209 ± 8.5
Annealed (fresh)	18.3 ± 0.16	0.911 ± 0.00	66.8 ± 0.75	11.1 ± 0.10	5.8 ± 0.25	789 ± 24.6
Annealed (aged)	16.0 ± 0.51	0.826 ± 0.02	50.4 ± 2.21	6.7 ± 0.20	13.3 ± 0.53	315 ± 28.3

cation. These devices were later exposed to continuous 1 sun illumination for a 5 hour time period and evaluated at regular intervals during the aging process. These devices are abbreviated as 'aged' devices. The *J–V* characteristic curves of both non-annealed and annealed, fresh and aged PBDB-T:ITIC devices, at room temperature under AM1.5G illumination at 100 mW cm^{-2}, are shown in Fig. 1d. The photovoltaic parameters extracted from Fig. 1d are summarized in Table 1.

The photovoltaic performances of the fresh non-annealed and annealed devices are similar, with a slightly higher fill factor (FF) in the non-annealed devices (68.8 ± 0.11%) compared to that of the annealed devices (66.8 ± 0.11%). A strong burn-in loss can be observed in all the major photovoltaic parameters (short-circuit current density (J_{sc}), open-circuit voltage (V_{oc}) and FF) of both non-annealed and annealed devices after continuous illumination for 5 hours. The reduction in V_{oc} is small (8–9%) and similar in all devices regardless of annealing. However, the photocurrent and FF losses are significant and the percentage of loss varies depending on the annealing conditions of the device. The reductions in J_{sc} and FF of the non-annealed devices after photo-aging are 20.8% and 34%, respectively, whereas in the annealed devices, they are 12.6% and 24.6%, respectively. As a result, the non-annealed aged devices lose more than half of their initial efficiencies, but the annealed devices are capable of retaining over 60% of their initial efficiencies. The burn-in degradation of PCE in PBDB-T:ITIC devices is higher than that in P3HT:$PC_{71}BM$ devices (PCE burn-in loss ~12% (ref. 34)), one of the most widely studied organic PSC systems,[35,36] but lower than that in PTB7:$PC_{71}BM$ devices (PCE burn-in loss ~61% (ref. 34)), which exhibit one of the highest PCEs in fullerene-based PSCs,[36,37] for the same illumination time period. Fig. 2a–d show the evolution of the photovoltaic parameters of PBDB-T:ITIC solar cells under continuous 1 sun equivalent illumination for 5 hours. It is clear that the annealed devices retain higher efficiencies after photo-degradation, compared to the non-annealed devices and the higher efficiencies are due to a higher degree of restoration of the initial J_{sc} and FF in the annealed devices. As the processing parameters and materials are identical for the non-annealed and annealed devices, including the electron transport layer (ETL)-ZnO, the improved burn-in loss of the annealed devices is attributed to the improved stability of the morphology of the donor–acceptor blend. This V_{oc} loss can be related to changes in both the active layer film,[27,38–40] and the interfacial properties.[23,41] The ZnO ETL is common within all devices; this ZnO/organic interface may cause a decrease in V_{oc}. Manor *et al.*[24] reported the formation of shunting channels in ZnO at the ZnO/organic interface following photo-aging under concentrated simulated sunlight, which reduces the hole blocking capacity of the ZnO layer and decreases the V_{oc} and to some extent, the FF of the degraded cells. Significant V_{oc} burn-in loss was also observed by Kam *et al.*[23] in organic BHJ devices with a ZnO ETL after the first 8 hours of continuous illumination. They too associated the degradation with a reduction in the hole blocking capacity of the ZnO ETL which they found to be caused by the UV portion of the spectrum. In this study, the V_{oc} loss in the annealed and non-annealed devices is comparable. Therefore, we believe that the dominant mechanism causing the V_{oc} loss and partial FF loss is related to the interfacial ZnO layer degradation and the loss of carrier selectivity. However, that does not explain the major J_{sc} and FF loss, which is more severe in the non-annealed devices. The J_{sc} and most FF losses suggest that the BHJ morphology of PBDB-T:ITIC might have changed drastically regardless of thermal annealing, however, it is expected that the annealed films are more ordered from a microstructure perspective, hence the losses are less severe in the corresponding aged devices.

To verify our hypothesis, PDS measurements of PBDB-T:ITIC blend films were carried out. The PDS technique is a direct measurement of optical absorption which is very sensitive to sub-band absorption.[20] It was used to measure the absorption coefficient of the fresh and aged active layer blends in the sub-bandgap region. The PBDB-T:ITIC films were deposited on quartz substrates, without any electrode deposition, and then were aged under light illumination of one-sun intensity in a similar manner to the complete solar cells. The PDS spectra of all the films are shown in Fig. 3. Fig. 3a and b represent the absorption spectra of the fresh and aged films for non-annealed and annealed conditions, respectively. In the figures, absorption in energies larger than the bandgap (~1.59 eV (ref. 19)) is caused by a band-to-band (HOMO–LUMO) transition. Absorption in this region can also be measured by traditional reflectance-and-transmittance (R&T) measurements. We have compared the results from PDS and R&T measurements (Fig. S1 and S2†). The R&T measurements closely match the PDS data above the bandgap energies, but the absorption from R&T measurements decreases sharply to zero near the bandgap energy due to the lack of sensitivity. In the sub-bandgap region, instead of becoming zero, the absorption reduces exponentially as the photon energy reduces. This exponential reduction in absorption coefficient is a typical feature close to the optical band gap of disordered semiconductors, such as organic semiconductors.[41] There is a clear trend of

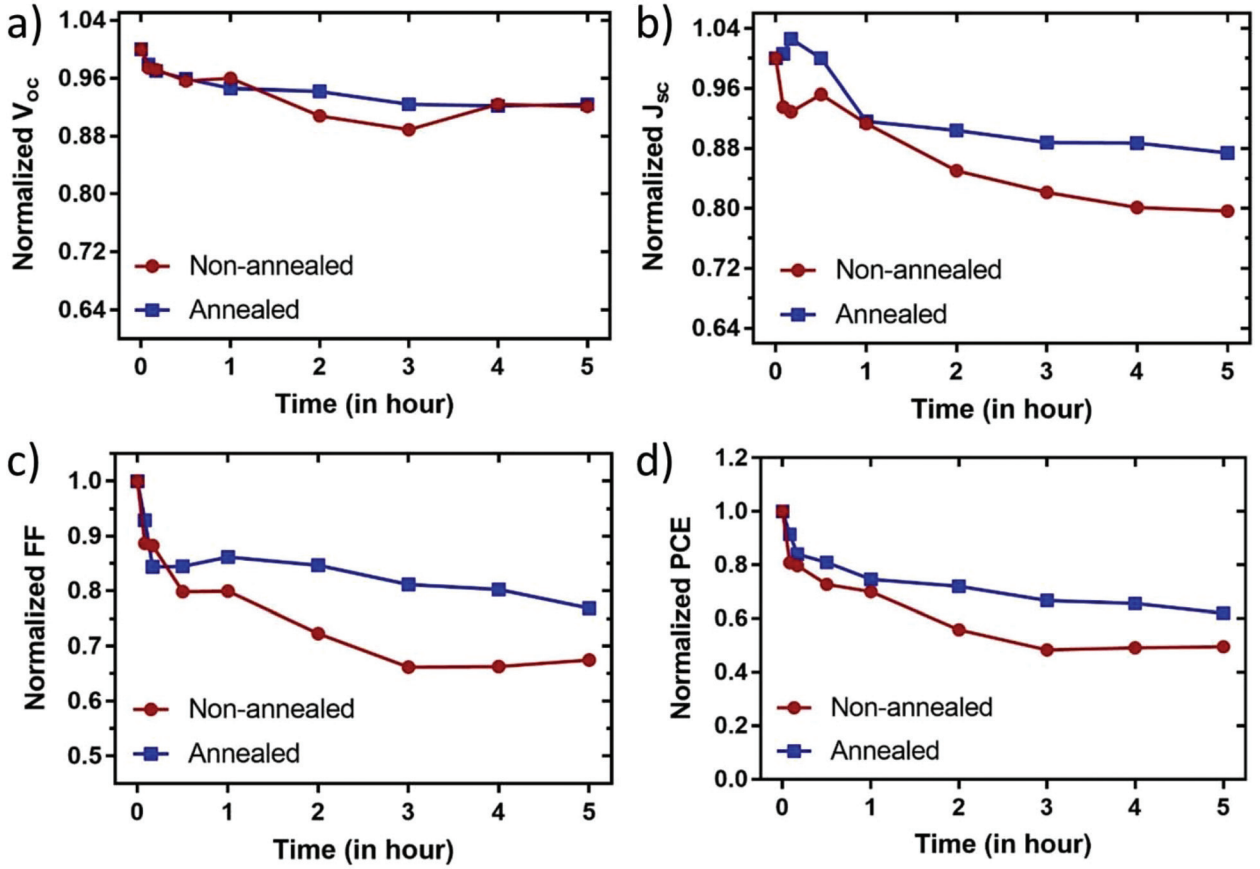

Fig. 2 Normalized photovoltaic parameters tracked over 5 hours of continuous illumination under AM1.5G illumination at 100 mW cm^{-2} for non-annealed and annealed PBDB-T:ITIC devices; (a) V_{oc}, (b) J_{sc}, (c) FF and (d) PCE *vs.* time in hour.

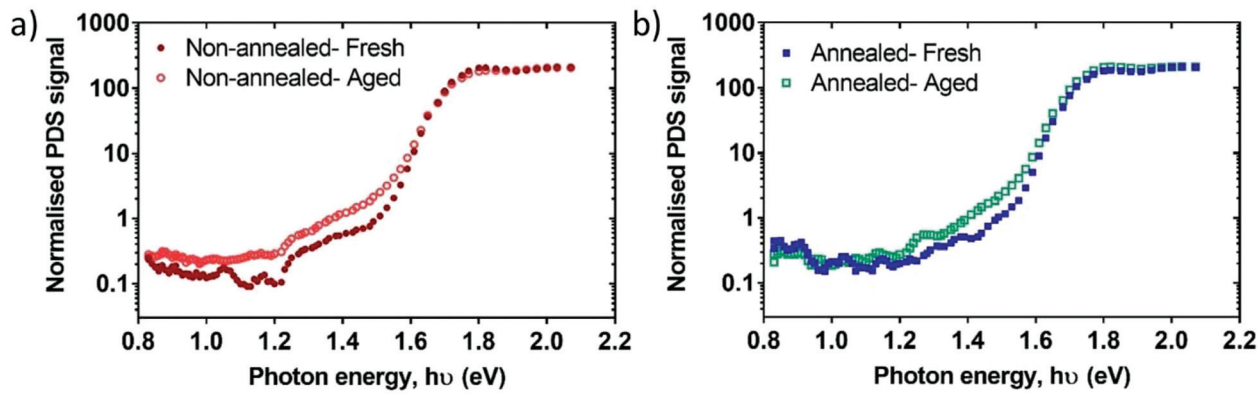

Fig. 3 Photothermal deflection spectroscopy (PDS) absorption spectra of (a) non-annealed and (b) annealed PBDB-T:ITIC BHJ blend films under both fresh and aged conditions. Absorption below 1.7 eV increased after photo-aging in both non-annealed and annealed films.

increase in sub-bandgap absorption after aging, in both non-annealed and annealed blend films. An Urbach tail model expressed by the following equation was used to calculate the Urbach energy for all the samples used in this work (both fresh and aged):[21,31]

$$\alpha = \alpha_0 \times e^{\frac{h\nu}{E_u}}, \quad (1)$$

where α_0 is a constant, h is the Planck's constant, ν is the frequency and E_u is the Urbach energy. A summary of the extracted Urbach energy values can be found in Table 2.

The magnitude of the Urbach energy is related to the width of the localized tail states at the absorption band-edge.[42,43] An increase in the Urbach energy indicates an increased energetic disorder within the semiconductor. It is clear from Table 2

Table 2 The list of Urbach energies of fresh and aged PBDB-T:ITIC films, both non-annealed and annealed, extracted from the sub-bandgap region (1.55–1.65 eV) in PDS

Film description	Urbach energy (meV)
Non-annealed (fresh)	34.4
Non-annealed (aged)	45.1
Annealed (fresh)	35.2
Annealed (aged)	42.9

that the Urbach energy of the PBDB-T:ITIC blend films increases after photo-aging, regardless of thermal annealing. There is a 31% increase in the Urbach energy of non-annealed films after photo-aging. In addition, in Fig. 3a, the aged non-annealed films have increased absorption at low photon energies (<1.3 eV) which is an indication of an increase in states in the bandgap of the BHJ blend in polymer solar cells.[27] These states can increase the energetic disorder in the active layer and thus reduce the device performance *via* trap mediated charge recombination.[27] This observation reinforces our hypothesis that the device performance is affected by the photo-degradation of the BHJ blend layer. Although there is no such difference in the absorption of fresh and aged annealed films at low photon energies (<1.3 eV), in the exponential region (1.55–1.65 eV), there is an increase in absorption in the aged annealed films which suggests an increase in Urbach energy (Fig. 3b). The broadening of Urbach energy in both non-annealed and annealed films is indicative of exponential distributions of localized states in the BHJ film after prolonged illumination which in turn is expected to increase the recombination losses inside the absorber and thus, reduce the J_{sc} and FF in the aged devices. However, for the annealed films, the increase in Urbach energy (22%) is lower than that for the non-annealed films (Table 2). The lower increase in E_u in the annealed films could stem from their initial higher degree of order due to thermal annealing. Ye *et al.*[44] observed that annealing contributed to an increase of the π–π stacking coherence length of the non-fullerene small molecule acceptors, such as IT-M and IT-DM, when mixed with the polymer, PBDB-T. The coherence length is a measure of the length scale over which a crystal lattice is expected to be preserved and expresses the extent of nanostructural order.[45] A higher coherence length reportedly benefits the charge transport characteristics of organic solar cells.[44,46] Hence, an increase in the π–π stacking coherence length of the annealed film is likely to increase the order by minimizing the number of defects and prevent the trapping of charge carriers.[45] We believe that due to the increased order in the annealed film, it exhibits a relatively low increase in Urbach energy and a higher retention of photovoltaic performance after photo-aging, although the photoinduced disorder cannot be prevented completely. In addition, the morphologies of the non-annealed and annealed PBDB-T:ITIC blend films were investigated using AFM, and the height and phase images (2 μm × 2 μm) are shown in Fig. S3.† The surface morphologies reveal that the blend film, after annealing, shows a smoother surface with small size aggregation which could also be a reason for the higher J_{sc} and FF[47] of the aged annealed devices.

To investigate the change in the electronic properties of the aged devices further, we have conducted EIS measurements of both the fresh and aged devices. EIS is a widely used tool in PSC characterization due to its ability to analyze the device charge transfer properties and distinguish different processes inside a complete working device according to the device's response to an externally applied alternating current (AC) signal.[22,29,48,49] Fig. 4 shows the Nyquist plots of the fabricated devices, before and after burn-in, from 100 Hz up to 1 MHz at 800 mV bias under dark. The impedance responses of all the devices (both fresh and aged) consist of semi-circles in a complex plane with the real part of the impedance ($Z'(\Omega)$) as the x-axis and the negative imaginary part ($-Z''(\Omega)$) as the y-axis. Generally, equivalent circuits are modelled to fit the experimental data in order to collect carrier transport information. All the Nyquist plots consist of two arcs at low and high frequency regions, which require two sets of parallel R–C elements to the model. From Fig. 4a and b, it can be observed that the low frequency arc, connected to the recombination resistance of the device,[35] of both the non-annealed and annealed devices reduces dramatically after burn-in. The measured Nyquist plots were then fitted with an equivalent electrical circuit, shown in the inset of Fig. 4(c). The equivalent circuit consists of two parallel R-CPE elements connected in series. Here, R represents the resistance and CPE (Constant Phase Element) is the non-ideal capacitance, related to non-homogeneities such as porosities and roughness.[36] R_s represents the series resistance that accounts for the resistance of metallic wires, and ohmic components, such as, ITO and Ag electrodes.[37] R_t is the resistance associated with electron transport through the interfacial layers and C_g is the geometric capacitance representing the dielectric component of the diode. The low frequency element of the impedance response is associated with the recombination resistance (R_{rec}) and chemical capacitance (C_μ) of the system.[50] R_{rec} is associated only with non-geminate recombination because the measurements were performed under dark conditions and no photo-carriers were generated.[32] C_μ is known as the distributed chemical capacitance.[37] In PSCs, the chemical capacitance is controlled by the charge carriers injected from the contact. The fitted electronic parameters of the equivalent circuits are listed in Table 3.

The series resistance value, R_s, is small, in the range of 1.3–1.5 Ω cm^2 and does not change after the burn-in process. The capacitances (C_g and C_μ) also do not change significantly due to the photo-degradation. However, the most notable change can be seen in the recombination resistance. The value of R_{rec} reduces drastically for both non-annealed and annealed aged devices. Under dark conditions, the charge carrier is injected from the external voltage supply only, hence the reduction in the recombination resistance for aged devices can be partially attributed to the increased charge trapping at the defect centers or dislocation states present at the interfaces between PBDB-T:ITIC blend films and neighboring charge

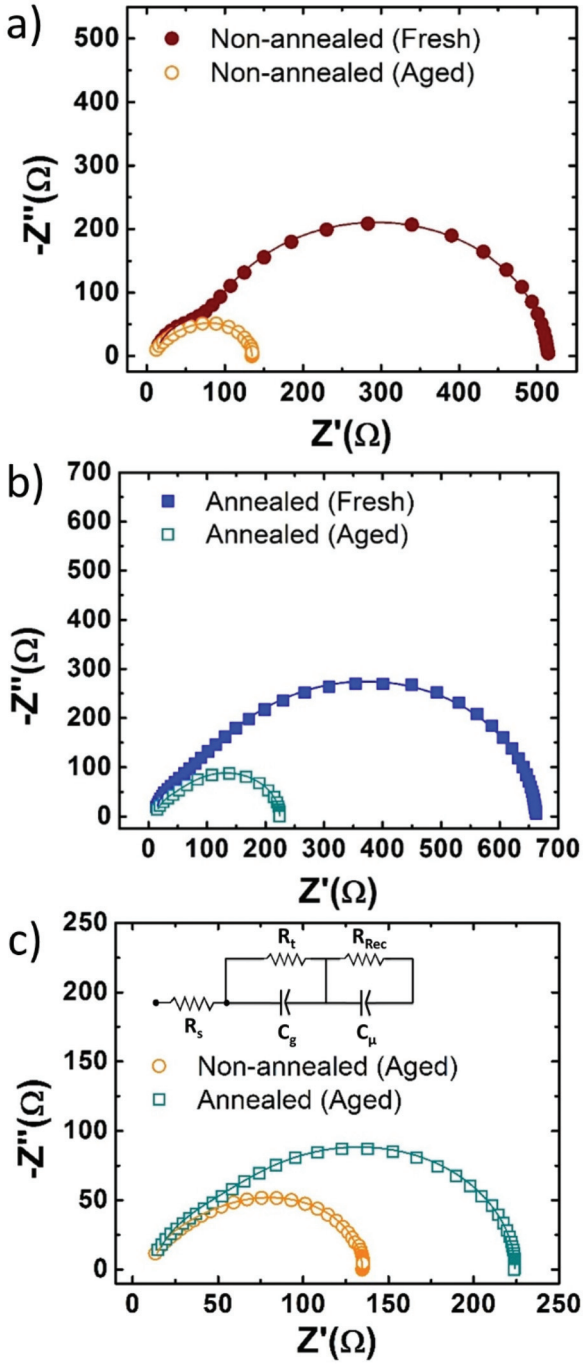

Fig. 4 Nyquist plot of (a) non-annealed and (b) annealed PBDB-T:ITIC devices at a bias of 800 mV under dark, before and after photodegradation; (c) comparison of impedance responses of the aged non-annealed and annealed devices.

selective contacts (ZnO/ITO and MoO_3/Ag). According to previous literature studies, the interfacial layers, such as ZnO, can also be sensitive to light illumination[23] and contain sub-bandgap states,[51] impeding efficient charge collection.[23,51,52] The change in R_{rec} will result from a combined effect of degradation of the active layer, as well as these interfacial effects.[53,54] Here, we have focused largely on the effect of the non-fullerene BHJ blend on the degradation of device performance. The trend in the reduction of R_{rec} of the aged devices matches with the increase in the Urbach energy of the aged BHJ blends (Table 2), hence it is expected that the recombination and charge collection processes are significantly influenced by the photo-degradation of the BHJ blend in the aged devices. The lower R_{rec} values of the aged devices are also consistent with the remarkably low shunt resistance (R_{sh}) values presented in Table 1. However, in a comparison between the aged non-annealed and annealed devices, the R_{rec} value of the annealed aged device (19.9 Ω cm^2) is almost two times higher than that of the non-annealed aged device (10.8 Ω cm^2) which is also clear from the corresponding Nyquist plots shown in Fig. 4c. We believe that the suppression of the carrier recombination phenomenon in the annealed aged devices is due to the inherent stability of the micromorphology of the active layer. The observation is also coherent with the relatively lower Urbach energy width of the annealed aged devices (Table 2). The fitted values of R_t show a similar trend to the R_{rec} values, the value of R_t decreases in the aged devices (both non-annealed and annealed). Table 3 displays the ratio of R_{rec} and R_t. The ratio (R_{rec}/R_t) also decreases in the aged devices which strongly correlates with the decrease in the FF of the respective aged device and indicates a poor charge collection efficiency.[39] Furthermore, the low frequency EIS spectra help in calculating the effective electron lifetime which is determined from the multiplication of R_{rec} and C_μ.[22] The electron lifetime, τ_n, expressed in μs (Table 3), also decreases dramatically after burn-in degradation which explains the decrease in the FF shown in Table 1.

In order to investigate the effect of photo-degradation on charge transfer in the PBDB-T:ITIC blend, the PL spectra of the non-annealed and annealed, fresh and aged films were recorded at different light intensities. All the recorded spectra are summarized in Fig. S4 and S5.† In all the cases, the PL intensity reduces gradually with the reduction in light intensity. For the sake of comparison, the PL spectra of the four types of films at the highest intensity are displayed in Fig. 5. The solid and dotted lines represent the fresh and aged films, respectively. The PL intensity of the non-annealed fresh film is higher than that of the annealed fresh film. Despite the difference in the PL intensity, the J_{sc} of the devices is similar. Hence, it is expected that the PL intensity of the non-annealed, fresh film increases due to the reduced non-radiative losses.[55] This observation is consistent with the slight increase in the fill factor[56] and concomitant device performance of the non-annealed, fresh devices. In both non-annealed and annealed films, the PL intensity decreased after photo-aging. In addition, the rate of reduction in PL intensity is higher in the non-annealed samples. In organic polymer donor and fullerene acceptor BHJ films, the decrease in PL intensity or so-called "PL quenching" occurs due to the efficient charge transfer between the polymer chains and fullerene molecules.[57–59] Similar quenching has also been observed in polymer–non-fullerene blends, which is attributed to the exciton dissociation due to the very efficient intermolecular charge trans-

Table 3 Fitted values of different electronic parameters from the Nyquist plots of the non-annealed and annealed OSCs under both fresh and aged conditions at an applied bias of 800 mV in the dark

Device description	R_s (Ω cm^2)	R_t (Ω cm^2)	R_{rec} (Ω cm^2)	R_{rec}/R_t	C_g (μF cm^{-2})	C_μ (μF cm^{-2})	Electron lifetime, τ_n (μs)
Non-annealed (fresh)	1.5	8.2	51.8	6.3	0.10	0.29	14.8
Non-annealed (aged)	1.5	3.9	10.8	2.8	0.18	0.30	3.2
Annealed (fresh)	1.3	11.7	66.5	5.7	0.11	0.19	12.9
Annealed (aged)	1.5	5.5	19.9	3.6	0.12	0.24	4.7

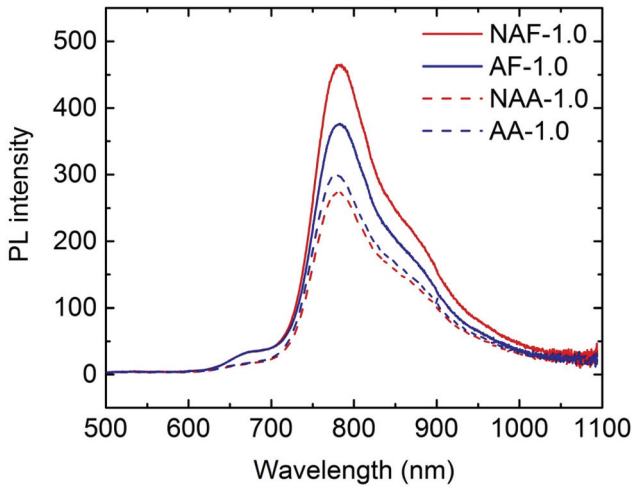

Fig. 5 PL emission spectra of the fresh and aged PBDB-T:ITIC BHJ blend films (both non-annealed and annealed).

fer from the polymer donor to the non-fullerene acceptor molecule.[38,60] In our case, although there was PL quenching in the aged film, there was no improvement in the J_{sc} of the respective aged devices. Hence, we assume that in the aged films, charge-carriers are recombining more *via* non-radiative pathways such as defect and trap centers in the bulk and at the interfaces. As a result, the number of total carriers recombining radiatively in fresh films is decreased in aged films; hence the decrease in PL intensity is due to the detrimental effect of photo-aging. This observation is in agreement with the findings from the PDS and EIS study leading to a reduction in device performance after photo-degradation.

4 Conclusions

In summary, we have studied the sensitivity of a BHJ organic solar cell, based on a novel polymer donor–non-fullerene acceptor combination (PBDB-T:ITIC), under the exposure of continuous 1 sun illumination. A significant decrease in the device efficiency was observed due to the degradation of both J_{sc} and FF, irrespective of thermal annealing treatment on the device. However, the degree of burn-in losses is slightly lower in the annealed devices. The underlying reasons for the photo-degradation are analyzed in detail in a systematic manner. The PDS measurements suggest that the observed decreases in J_{sc} and FF are due to the broadening of Urbach energy and a subsequent increase in the energetic disorder in the active layer. Photochemical reactions increase the exponential distributions of localized states in aged PBDB-T:ITIC films, creating trap-mediated recombination centers. The resulting disorder in the active layer negatively affected the charge transfer properties of the fabricated devices. The EIS analysis showed a drastic reduction in the device recombination resistance (R_{rec}). Under dark conditions, the injected carriers were trapped in the defect centers at the active layer (PBDB-T:ITIC blend film)/charge transport layer (ZnO/ITO and MoO_3/Ag) interfaces. A reduction in the radiative recombination of the aged active layer film (PL quenching) confirms that the recombination occurs *via* non-radiative pathways. The demonstrated burn-in loss at the very beginning of the device operation lifetime needs to be properly addressed and eliminated in order to fully utilize the benefit of excellent efficiency of the new generation high-performance PSC in future applications.

Conflicts of interest

There are no conflicts to declare.

Acknowledgements

The authors would like to thank the Australian Centre for Advanced Photovoltaics, UNSW staff and technicians for their support. We are grateful to all of our OPV group members for useful discussions and support during this work. We acknowledge Future Solar Technologies for providing funding. We also thank Jialiang Huang and Binesh Puthen-Veettil for useful scientific discussion.

References

1 M. Kaltenbrunner, M. S. White, E. D. Głowacki, T. Sekitani, T. Someya, N. S. Sariciftci and S. Bauer, *Nat. Commun.*, 2012, **3**, 770.
2 W. Yu, X. Jia, Y. Long, L. Shen, Y. Liu, W. Guo and S. Ruan, *ACS Appl. Mater. Interfaces*, 2015, **7**, 9920–9928.
3 M. B. Upama, M. Wright, N. K. Elumalai, M. A. Mahmud, D. Wang, K. H. Chan, C. Xu, F. Haque and A. Uddin, *Curr. Appl. Phys.*, 2017, **17**, 298–305.
4 Q.-D. Ou, H.-J. Xie, J.-D. Chen, L. Zhou, Y.-Q. Li and J.-X. Tang, *J. Mater. Chem. A*, 2016, **4**, 18952–18962.

5 R. Søndergaard, M. Hösel, D. Angmo, T. T. Larsen-Olsen and F. C. Krebs, *Mater. Today*, 2012, **15**, 36–49.
6 F. C. Krebs, S. A. Gevorgyan and J. Alstrup, *J. Mater. Chem.*, 2009, **19**, 5442–5451.
7 F. C. Krebs, *Sol. Energy Mater. Sol. Cells*, 2009, **93**, 394–412.
8 W. Zhao, S. Li, H. Yao, S. Zhang, Y. Zhang, B. Yang and J. Hou, *J. Am. Chem. Soc.*, 2017, **139**, 7148–7151.
9 B. C. Thompson and J. M. J. Fréchet, *Angew. Chem., Int. Ed.*, 2008, **47**, 58–77.
10 L.-M. Chen, Z. Hong, G. Li and Y. Yang, *Adv. Mater.*, 2009, **21**, 1434–1449.
11 Y. He and Y. Li, *Phys. Chem. Chem. Phys.*, 2011, **13**, 1970–1983.
12 Y. Qin, M. A. Uddin, Y. Chen, B. Jang, K. Zhao, Z. Zheng, R. Yu, T. J. Shin, H. Y. Woo and J. Hou, *Adv. Mater.*, 2016, **28**, 9416–9422.
13 L. Yang, S. Zhang, C. He, J. Zhang, H. Yao, Y. Yang, Y. Zhang, W. Zhao and J. Hou, *J. Am. Chem. Soc.*, 2017, **139**, 1958–1966.
14 H. Bin, Z.-G. Zhang, L. Gao, S. Chen, L. Zhong, L. Xue, C. Yang and Y. Li, *J. Am. Chem. Soc.*, 2016, **138**, 4657–4664.
15 C. B. Nielsen, S. Holliday, H.-Y. Chen, S. J. Cryer and I. McCulloch, *Acc. Chem. Res.*, 2015, **48**, 2803–2812.
16 T. Kim, J.-H. Kim, T. E. Kang, C. Lee, H. Kang, M. Shin, C. Wang, B. Ma, U. Jeong, T.-S. Kim and B. J. Kim, *Nat. Commun.*, 2015, **6**, 8547.
17 Y. Lin, J. Wang, Z.-G. Zhang, H. Bai, Y. Li, D. Zhu and X. Zhan, *Adv. Mater.*, 2015, **27**, 1170–1174.
18 W. Zhao, D. Qian, S. Zhang, S. Li, O. Inganäs, F. Gao and J. Hou, *Adv. Mater.*, 2016, **28**, 4734–4739.
19 H. Bin, L. Gao, Z.-G. Zhang, Y. Yang, Y. Zhang, C. Zhang, S. Chen, L. Xue, C. Yang, M. Xiao and Y. Li, *Nat. Commun.*, 2016, **7**, 13651.
20 C. Yan, K. Sun, J. Huang, S. Johnston, F. Liu, B. P. Veettil, K. Sun, A. Pu, F. Zhou, J. A. Stride, M. A. Green and X. Hao, *ACS Energy Lett.*, 2017, **2**, 930–936.
21 S. J. Ikhmayies and R. N. Ahmad-Bitar, *J. Mater. Res. Technol.*, 2013, **2**, 221–227.
22 G. Garcia-Belmonte, P. P. Boix, J. Bisquert, M. Sessolo and H. J. Bolink, *Sol. Energy Mater. Sol. Cells*, 2010, **94**, 366–375.
23 Z. Kam, X. Wang, J. Zhang and J. Wu, *ACS Appl. Mater. Interfaces*, 2015, **7**, 1608–1615.
24 A. Manor, E. A. Katz, T. Tromholt and F. C. Krebs, *Adv. Energy Mater.*, 2011, **1**, 836–843.
25 S. Holliday, R. S. Ashraf, A. Wadsworth, D. Baran, S. A. Yousaf, C. B. Nielsen, C.-H. Tan, S. D. Dimitrov, Z. Shang, N. Gasparini, M. Alamoudi, F. Laquai, C. J. Brabec, A. Salleo, J. R. Durrant and I. McCulloch, *Nat. Commun.*, 2016, **7**, 11585.
26 Y. Lin, F. Zhao, Q. He, L. Huo, Y. Wu, T. C. Parker, W. Ma, Y. Sun, C. Wang, D. Zhu, A. J. Heeger, S. R. Marder and X. Zhan, *J. Am. Chem. Soc.*, 2016, **138**, 4955–4961.
27 C. H. Peters, I. T. Sachs-Quintana, W. R. Mateker, T. Heumueller, J. Rivnay, R. Noriega, Z. M. Beiley, E. T. Hoke, A. Salleo and M. D. McGehee, *Adv. Mater.*, 2012, **24**, 663–668.
28 M. O. Reese, S. A. Gevorgyan, M. Jørgensen, E. Bundgaard, S. R. Kurtz, D. S. Ginley, D. C. Olson, M. T. Lloyd, P. Morvillo, E. A. Katz, A. Elschner, O. Haillant, T. R. Currier, V. Shrotriya, M. Hermenau, M. Riede, K. R. Kirov, G. Trimmel, T. Rath, O. Inganäs, F. Zhang, M. Andersson, K. Tvingstedt, M. Lira-Cantu, D. Laird, C. McGuiness, S. Gowrisanker, M. Pannone, M. Xiao, J. Hauch, R. Steim, D. M. DeLongchamp, R. Rösch, H. Hoppe, N. Espinosa, A. Urbina, G. Yaman-Uzunoglu, J.-B. Bonekamp, A. J. J. M. van Breemen, C. Girotto, E. Voroshazi and F. C. Krebs, *Sol. Energy Mater. Sol. Cells*, 2011, **95**, 1253–1267.
29 G. Garcia-Belmonte, A. Guerrero and J. Bisquert, *J. Phys. Chem. Lett.*, 2013, **4**, 877–886.
30 E. Voroshazi, I. Cardinaletti, T. Conard and B. P. Rand, *Adv. Energy Mater.*, 2014, **4**, 1400848.
31 M. B. Upama, M. Wright, B. Puthen-Veettil, N. K. Elumalai, M. A. Mahmud, D. Wang, K. H. Chan, C. Xu, F. Haque and A. Uddin, *RSC Adv.*, 2016, **6**, 103899–103904.
32 M. B. Upama, N. K. Elumalai, M. A. Mahmud, M. Wright, D. Wang, C. Xu, F. Haque, K. H. Chan and A. Uddin, *Appl. Surf. Sci.*, 2017, **416**, 834–844.
33 M. B. Upama, M. Wright, N. K. Elumalai, M. A. Mahmud, D. Wang, K. H. Chan, C. Xu, F. Haque and A. Uddin, *Opt. Quantum Electron.*, 2017, **49**, 28.
34 M. B. Upama, N. Elumalai, M. A. Mahmud, H. Sun, D. Wang, K. H. Chan, M. Wright, C. Xu and A. Uddin, *Thin Solid Films*, 2017, **636**, 127–136.
35 P. P. Boix, Y. H. Lee, F. Fabregat-Santiago, S. H. Im, I. Mora-Sero, J. Bisquert and S. I. Seok, *ACS Nano*, 2012, **6**, 873–880.
36 B. Arredondo, B. Romero, G. Del Pozo, M. Sessler, C. Veit and U. Würfel, *Sol. Energy Mater. Sol. Cells*, 2014, **128**, 351–356.
37 A. Aprilia, P. Wulandari, V. Suendo, Herman, R. Hidayat, A. Fujii and M. Ozaki, *Sol. Energy Mater. Sol. Cells*, 2013, **111**, 181–188.
38 O. Y. Park, H. U. Kim, J.-H. Kim, J. B. Park, J. Kwak, W. S. Shin, S. C. Yoon and D.-H. Hwang, *Sol. Energy Mater. Sol. Cells*, 2013, **116**, 275–282.
39 L. Xu, Y.-J. Lee and J. W. P. Hsu, *Appl. Phys. Lett.*, 2014, **105**, 123904.
40 A. Sadhanala, F. Deschler, T. H. Thomas, S. E. Dutton, K. C. Goedel, F. C. Hanusch, M. L. Lai, U. Steiner, T. Bein, P. Docampo, D. Cahen and R. H. Friend, *J. Phys. Chem. Lett.*, 2014, **5**, 2501–2505.
41 W. Gong, M. A. Faist, N. J. Ekins-Daukes, Z. Xu, D. D. C. Bradley, J. Nelson and T. Kirchartz, *Phys. Rev. B: Condens. Matter*, 2012, **86**, 024201.
42 M. Abdi-Jalebi, M. I. Dar, A. Sadhanala, S. P. Senanayak, F. Giordano, S. M. Zakeeruddin, M. Grätzel and R. H. Friend, *J. Phys. Chem. Lett.*, 2016, **7**, 3264–3269.
43 S. Dutta, S. Chattopadhyay, A. Sarkar, M. Chakrabarti, D. Sanyal and D. Jana, *Prog. Mater. Sci.*, 2009, **54**, 89–136.
44 L. Ye, W. Zhao, S. Li, S. Mukherjee, J. H. Carpenter, O. Awartani, X. Jiao, J. Hou and H. Ade, *Adv. Energy Mater.*, 2017, **7**, 1602000.

45 A. T. Yiu, P. M. Beaujuge, O. P. Lee, C. H. Woo, M. F. Toney and J. M. J. Fréchet, *J. Am. Chem. Soc.*, 2012, **134**, 2180–2185.
46 W. Li, S. Albrecht, L. Yang, S. Roland, J. R. Tumbleston, T. McAfee, L. Yan, M. A. Kelly, H. Ade, D. Neher and W. You, *J. Am. Chem. Soc.*, 2014, **136**, 15566–15576.
47 W. Zhao, S. Zhang and J. Hou, *J. Sci. China Chem.*, 2016, **59**, 1574–1582.
48 J. Bisquert, *Phys. Rev. B: Condens. Matter Mater. Phys.*, 2008, **77**, 235203.
49 J. Bisquert and G. Garcia-Belmonte, *J. Phys. Chem. Lett.*, 2011, **2**, 1950–1964.
50 D. Liu, J. Yang and T. L. Kelly, *J. Am. Chem. Soc.*, 2014, **136**, 17116–17122.
51 B. Wu, Z. Wu, Q. Yang, F. Zhu, T.-W. Ng, C.-S. Lee, S.-H. Cheung and S.-K. So, *ACS Appl. Mater. Interfaces*, 2016, **8**, 14717–14724.
52 Z. Wu, B. Wu, H. L. Tam and F. Zhu, *Org. Electron.*, 2016, **31**, 266–272.
53 W. L. Leong, S. R. Cowan and A. J. Heeger, *Adv. Energy Mater.*, 2011, **1**, 517–522.
54 F. Fabregat-Santiago, G. Garcia-Belmonte, I. Mora-Sero and J. Bisquert, *Phys. Chem. Chem. Phys.*, 2011, **13**, 9083–9118.
55 L. Zuo, H. Guo, D. W. deQuilettes, S. Jariwala, N. De Marco, S. Dong, R. DeBlock, D. S. Ginger, B. Dunn, M. Wang and Y. Yang, *Sci. Adv.*, 2017, **3**, 1700106.
56 S. R. Cowan, A. Roy and A. J. Heeger, *Phys. Rev. B: Condens. Matter Mater. Phys.*, 2010, **82**, 245207.
57 Z. Jin and J. Wang, *Sci. Rep.*, 2014, **4**, 5331.
58 M. Campoy-Quiles, Y. Kanai, A. El-Basaty, H. Sakai and H. Murata, *Org. Electron.*, 2009, **10**, 1120–1132.
59 S. S. van Bavel, M. Bärenklau, G. de With, H. Hoppe and J. Loos, *Adv. Funct. Mater.*, 2010, **20**, 1458–1463.
60 Suman, A. Bagui, V. Gupta, K. K. Maurya and S. P. Singh, *J. Phys. Chem. C*, 2016, **120**, 24615–24622.